SISSA

PAPER • OPEN ACCESS

Radiation hardness study of the ePix100 sensor and ASIC under direct illumination at the European XFEL

To cite this article: I. Klačková *et al* 2021 *JINST* **16** P09009

View the article online for updates and enhancements.

Radiation hardness study of the ePix100 sensor and ASIC under direct illumination at the European XFEL

I. Klačková,[a,b,*] **K. Ahmed,**[a] **G. Blaj,**[c] **M. Cascella,**[a] **V. Cerantola,**[a] **C. Chang,**[c] **A. Dragone,**[c] **S. Göde,**[a] **S. Hauf,**[a] **C. Kenney,**[c] **J. Segal,**[c] **M. Kuster**[a] **and A. Šagátová**[b]

[a]*European XFEL,*
 Holzkoppel 4, 22869 Schenefeld, Germany

[b]*Slovak University of Technology, Faculty of Electrical Engineering and Information Technology,*
 Ilkovičova 3, 81219 Bratislava, Slovakia

[c]*SLAC National Accelerator Laboratory,*
 Sand Hill Road 2575, Menlo Park, California 94025, U.S.A.

 E-mail: ivana.klackova@xfel.eu

*Corresponding author.

2021 JINST 16 P09009

ABSTRACT: The ePix detector family provides multiple variants of hybrid pixel detectors to support a wide range of applications at free electron laser (FEL) facilities. The ePix detectors are by design versatile and easily re-configurable camera systems with common mechanical, electrical and data acquisition interfaces. Operation of detectors at FEL sources providing high brilliance, high repetition rate and ultra-short X-ray pulses poses a high risk of radiation damage to exposed detector components, such as the sensor and the readout Application Specific Integrated Circuit (ASIC). Knowledge about radiation-induced damage is important for understanding its influence on the quality of scientific data and the lifetime of the detector.

We present the results of a systematic study of the influence of radiation-induced damage on the performance and lifetime of an ePix100a detector module using a direct attenuated beam of the European X-ray Free Electron Laser Facility (European XFEL) at 9 keV photon energy and average power of 10 μW. An area of 20 pixels × 20 pixels was irradiated with an average photon flux of $\approx 7 \times 10^9$ photons/s to a dose of approximately (760±65) kGy at the location of the Si/SiO_2 interfaces in the sensor.

A dose dependent increase in both offset and noise of the ePix100a detector have been observed originating from an increase of the sensor leakage current. Moreover, we observed an effect directly after irradiation resulting in the saturation of individual pixels by their dark current. Changes in gain are evaluated one and half hours post-irradiation and suggest damage to occur also on the ASIC level. Based on the obtained results, thresholds for beam parameters are deduced and the detector lifetime is estimated with respect to the requirements to the data quality in order to satisfy the scientific standards defined by the experiments. We conclude the detector can withstand a beam with an energy up to 1 μJ at a photon energy of 9 keV impacting on an area of 1 mm^2. The detector can be used without significant degradation of its performance for several years if the incident photon beam intensities do not exceed the detector's dynamic range by at least three orders of magnitude. Our results provide valuable input for the operation of the ePix100a detector at FEL facilities and the design of future detector technology.

Contents

1 Introduction

To fully exploit the research and scientific possibilities of the European XFEL [1], novel detectors have been developed in order to satisfy the challenging FEL requirements, e.g. single photon sensitivity at the specified energy range, time resolution at the level of individual FEL pulses or a high dynamic range [2, 3]. The European XFEL is a high repetition rate facility, delivering pulse trains with a repetition rate of 10 Hz. Every train contains up to 2700 high intensity X-ray pulses separated by 220 ns each. An X-ray beam with such characteristics poses a high risk of damaging the detector systems by radiation, thus creates the need for radiation hard detectors. For a detector operated in a scattering geometry close to the sample and being directly illuminated by scattered X-rays, the absorbed doses can amount to up to 1 GGy using a silicon sensor of 500 μm thickness when considering three years of facility operation [2]. While some of the European XFEL detectors have been optimized to incorporate a higher level of radiation hardness into their design, e.g. the Adaptive Gain Integrating Detector (AGIPD) [4] and the Large Pixel Detector (LPD) [5], other detectors, not specifically built for operation at the European XFEL, have been tested for and offer a certain level of radiation tolerance, e.g. the JUNGFRAU [6] detector. The ePix100a detector, designed for applications at FEL facilities [7] was studied to evaluate its radiation hardness at the

European XFEL. The aim of the presented study is to determine the level of damage caused by the X-ray laser beam, understand and characterize the radiation-induced damage effects and validate their impact on the quality of scientific data.

2 Radiation-induced damage effects on silicon detectors

Operating silicon sensors in the harsh radiation environment of FELs can have severe implications on a detectors' performance and its lifetime. Due to their high peak brilliance, FELs can deliver up to 10^{12} photons/pulse to the sample interaction region. Due to the direct X-ray illumination of the sensor, radiation tolerance of the sensor and Application Specific Integrated Circuit (ASIC) are of high importance. Sensors based on metal-oxide-semiconductor (MOS) structures, where charge flow takes place close to the surface, are known to be especially sensitive to damage induced by ionizing radiation. Therefore, thorough studies of the influence of the FEL radiation on silicon sensors have been conducted during the design and development phase of the first generation MHz detectors for the European XFEL. Results reported by Zhang et al. [4, 8, 9] give insight on the parameters determining the damage depending on the delivered dose and their influence on the operation of different silicon sensor designs. These studies provided valuable input for detector designs minimizing radiation damage effects and optimization of sensor operation parameters as reported by Schwandt et al. [10, 11]. Klanner et al. [12] provide an exemplary overview of the AGIPD detector [13] related sensor design challenges. The studies cited above provide useful knowledge and valuable observations for the here presented experiment results.

In general two fundamentally different damage mechanisms dominate the radiation/particle interaction with silicon. These are displacement damage (bulk damage) and surface damage. Bulk damage results in point defects (Frenkel-pairs) or agglomeration of defects caused by highly energetic hadrons, leptons or higher energetic gamma rays knocking out the primary atom from its lattice position (interstitial) through a non-ionizing (NIEL) interaction [14, 15]. The displacement energy E_d required to create such a defect is in the range between 10 eV and 36 eV [16, 17]. E_d depends amongst other parameters on the lattice orientation. Since the energy transfer of a photon with an energy less than 20 keV to the silicon atom is significantly below E_d, displacement damage is negligible at these photon energies. Consequently, surface damage is the dominating damage mechanism of relevance for our study.

In contrast to bulk damage, surface damage originates in ionization energy losses of X-ray photons or charged particles and subsequently leads to an accumulation of space charges in or close to an interface between e.g. an insulating or dielectric layer and silicon [18]. A typical example are interfaces between SiO_2 and silicon when SiO_2 is used as gate oxide or field oxide as an insulating layer between semiconductor structures. The density of the created space charge is proportional to the amount of energy absorbed at or close to the interface. The accumulation of space charge in turn can significantly influence the performance properties of the sensor, like leakage current, noise and dynamic range. For an in-depth overview of surface damage mechanisms, we refer the reader to the available literature [19–21] and references therein.
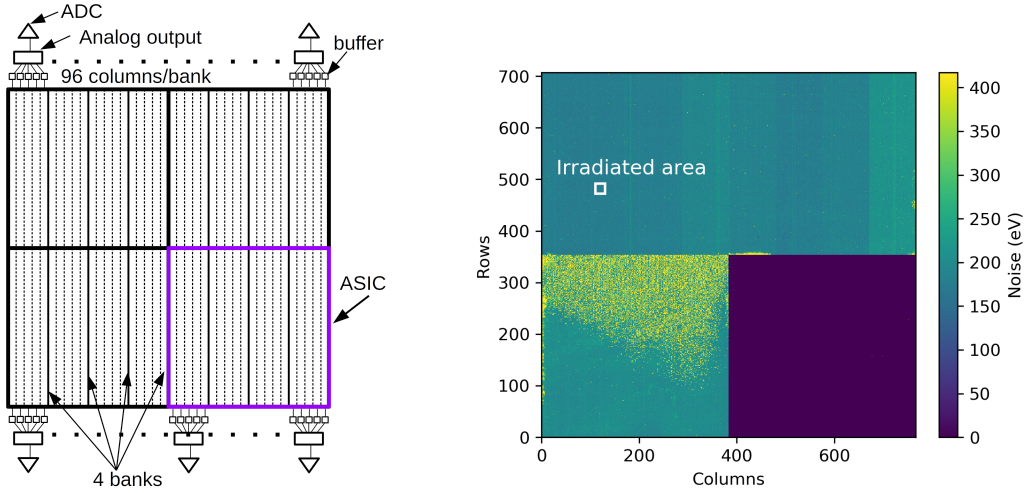
Figure 1. Left: schematic view of the ePix100a sensor as seen from the experiment's interaction region, showing the location of the signal readout nodes, the arrangement of the 4 ASICs required to read out one sensor module with a size of 352 pixels × 384 pixels. Each ASIC is divided into four banks accommodating 96 columns multiplexed to a single analog output digitized by an external ADC. Four sensor modules and their ASICs are arranged in a rectangular geometry to build one complete detector module consisting of 704 pixels × 768 pixels. Right: noise map of the ePix100a visualizing placement and size of the area irradiated by the FEL beam (white square). The area on the bottom left is showing a higher noise level in comparison to the two modules on the top. The bottom right module is not providing data. The image qualitatively illustrates the performance before irradiation.

3 The ePix100a detector module

The ePix100a is a backside illuminated direct detection hybrid pixel detector optimized for low noise applications in the energy range between 2 keV and 18 keV [22]. The ePix detector family is based on a modular design, where each ePix100a detector module consists of a fully depleted silicon sensor, which is flip-chip bonded to 4 ePix ASICs, and connected to front-end electronics, the cooling system, its mechanics and housing.

One single ASIC provides the readout and signal processing architecture for a sensor region of 352 pixels × 384 pixels, each of a size of 50 μm × 50 μm. The analog signal provided by a sensor pixel is processed by a low noise charge integrator and subsequently, low pass filtered before the signal passes a correlated double sampling (CDS) stage for baseline correction and noise filtering and is finally stored in a buffer. Further processing of the analog signal is organised in a column parallel fashion. The analog output of the pixels of one bank accommodating 96 columns is multiplexed to a single analog output node before it is digitized by an external 14 bit sigma-delta analog to digital converter (ADC). Figure 1 (left panel) illustrates the geometric arrangement of the readout banks and the ADCs. The analog output nodes are arranged on the top and bottom sides of the ASICs and sensor. An overview of the ePix100a ASIC pixel layout is schematically shown in the left part of figure 2. The dynamic range of the ePix100a detector, defined by the number of ADC digitisation levels available for photon detection, allows to measure up to 220 ke⁻ ≈ 100 × 8 keV photons per pixel at a maximum frame rate of 240 Hz. For a detailed description of the ePix ASIC, detector
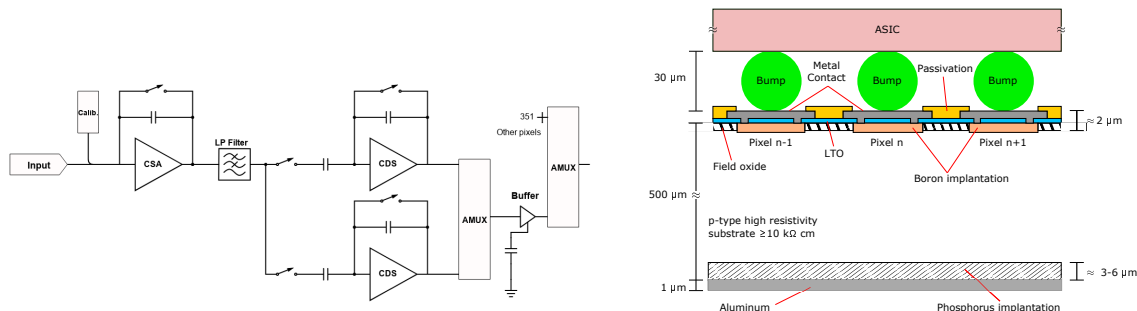
Figure 2. Left: schematic drawing of the ePix100a ASIC pixel layout. Right: Schematic view of the ePix100a sensor cross-section including interconnection bump bonds and the readout ASIC. The sensor is illuminated from the backside, i.e. from the bottom. Please note that this drawing is not to scale.

design and a performance review, we refer the interested reader to Markovic et al. [23], Blaj et al. [22] and Nishimura et al. [24].

Figure 2 (right panel) shows a schematic view of the vertical cross-section of the ePix100a sensor produced by SINTEF. The photon entrance window is coated with aluminum acting as a light-blocking filter for optical, UV and IR light. The bulk of the sensor is made of p-doped high resistivity < 100 > silicon. Due to its backside-illuminated design, structures potentially vulnerable to radiation damage, i.e. interfaces to the Low Temperature Oxide (LTO) and Field Oxide, are located on the front side of the chip. The interconnection between the sensor and ASIC is provided through 30 μm large solder bump bonds attached to Ti/Cu metal gates. The pixels and guard rings are biased through the ASIC. The 500 μm thick sensor enables the detection of X-ray photons with energies between 3 keV and 13 keV with a quantum efficiency $\geq 80\%$ and at the same time efficiently shields the underlying ASIC from X-ray radiation at low photon energies. The ePix100a camera is currently being used at the High Energy Density (HED) instrument [25] and Material Imaging and Dynamics (MID) [26, 27] instrument at the European XFEL.

4 Experiment setup and methodology

The radiation damage study was performed at the HED instrument at the European XFEL. The HED instrument can provide a beam of photon pulses with an energy between 5 keV and 20 keV and a maximum pulse energy of approximately 1 mJ [25]. For our study, we used an ePix100a test module equipped with four ASICs and arranged as shown in figure 1. Two of the ASICs were fully functional (area on the top left and right shown in the right image of figure 1), one had a significantly higher mean noise before irradiation (image area on the bottom left part of the same image) and one was unresponsive (bottom right part of the image). The beam spot, having an area of approximately 1 mm^2 and covering approximately 20 pixels × 20 pixels of the ePix100a sensor, was used to irradiate the area with the lowest pre-irradiation noise referred to as a region of interest (ROI) during the remainder of this publication (see figure 1, right panel).

Exposing the detector to the direct beam could cause instantaneous and permanent physical damage to the sensor, e.g. by ablation or melting of the sensor material. As shown by Koyama et al. [28], the silicon ablation threshold for a 10 keV photon is $E_{th} = 0.78\,\mu J/\mu m^2$. To avoid this kind

of damage, we initially attenuated the FEL beam to energies well below E_{th} with a configurable stack of Chemical Vapor Deposition (CVD) diamond and Si foils of various thicknesses available at the instrument. Apart from physical damage to the sensor surface, components of the pixel ASIC could be damaged by irradiation with excessive beam energies, as the ASIC [23, 29] does not implement protection circuitry for signals significantly above the detector's dynamic range. To find a beam energy, which on the one hand is sufficient to achieve the anticipated dose rate of 200 kGy/h and at the same time allows safe operation of the detector, we step by step gradually reduced the absorption of the stack until we found a configuration which allowed us to illuminate the detector up to an exposure time of > 5 min without observing failure of the irradiated pixels. By following this procedure, we found that the ePix100a pixels can withstand beam energies of up to 1 μJ for longer time periods without individual pixels experiencing permanent failure. Hence, we irradiated the sensor with a beam energy of 1 μJ. As discussed later in the text, beam energy of 1 μJ causes pixels to become unresponsive during the duration of irradiation, but it does not cause permanent failure of the irradiated pixels. This beam energy setting was used deliberately to trigger pixels unresponsiveness to allow for beam position tracking (explained in section 4.2).

The beam energy was continuously monitored with the X-ray Gas Monitors (XGM) installed at the HED instrument throughout our study (see [30, 31] for a technical description of and details about the performance of the European XFEL photon diagnostic XGMs). The XGMs are capable of non-invasively measuring the single X-ray pulse energy with an absolute accuracy of $7\% - 10\%$ depending on the measured signal strength and to provide a beam position measurement with precision between 10 μm and 50 μm if the beam position stays within ±6 mm of the absolutely calibrated reference position. In addition to the diagnostic information provided by the XGMs, we used the ePix100a detector to measure the X-ray spot position and potential drifts of the X-ray spot. A schematic view of the experiment setup is shown in figure 3.

To monitor the system noise, leakage current, gain and energy resolution of the detector, we acquired pre- and post-irradiation calibration data with $t_{Int} = 50$ μs consisting of dark and flat-field measurements. The flat-field measurements were performed by homogeneously illuminating the ePix100a with Cu-K$_\alpha$ fluorescence photons originating in a 50 μm thick copper foil which could be moved into the FEL beam. To acquire dark data the FEL beam was blocked and the detector was located in the flat-field configuration in the dark HED vacuum chamber (see figure 3), excluding illumination with visible light. A summary of the FEL beam and detector parameters used during our experiment is provided in table 1. Operational constraints prevented us from taking calibration data more frequently, e.g. after the completion of each individual irradiation cycle. Noise and offset were monitored on an hourly time scale shorty after the last irradiation cycle and later on, on time scales of days after the self-annealing effects slowly started to reduce in significance.

We irradiated the ePix100a module with an attenuated beam of 9 keV photons. The facility was set up to deliver 100 pulses per pulse train (i.e. 100 pulses per 100 ms). We operated the detector with a frame rate of 10 Hz, corresponding to the typical use case of the ePix100a detector at the European XFEL. The irradiation was performed in cycles of 20 min long individual exposures. Radiation-induced changes of the noise and offset were monitored regularly between two consecutive cycles with two different integration time settings, $t_{Int} = 50$ μs and $t_{Int} = 800$ μs. The choice of the 800 μs long integration time is motivated by the higher sensitivity to potentially very small changes of the leakage current, which would manifest through a proportional change of the offset. On the other

Table 1. Summary of the detector operation and beam line parameters as used during our irradiation experiment.

Beam parameters	
Average beam energy at the detector	10 nJ/Pulse
Photon energy	9 keV
Number of X-ray pulses per pulse train	100 Pulses
Dose rate at the Si/SiO_2 interfaces	200 kGy/h
Beam intensity monitoring	XGMs at HED beamline
Detector parameters	
Pixel size	50 μm × 50 μm
Sensor size	704 pixels × 768 pixels
Sensor thickness (depleted bulk)	500 μm
Irradiated sensor area	20 pixels × 20 pixels (1 mm^2)
Full well capacity	220 ke$^-$
Frame rate	10 Hz
Integration time	50 μs and 800 μs
Bias voltage	200 V
Sensor temperature	−9° C
Operating pressure	$\leq 1 \times 10^{-5}$ mbar

hand, $t_{Int} = 50$ μs is a typical value used during scientific experiments at HED. In total we executed 14 such irradiation cycles in the course of our study. During each cycle, we achieved a typical dose rate of (204 ± 18) kGy/h translated to the depth of the Si/SiO_2 interfaces in the sensor. We determined the dose rate with a Monte Carlo simulation using the measured average photon flux at the ePix100a sensor surface and the sensor geometry as input parameters, as discussed extensively in section 4.2.

Throughout our irradiation cycles, the detector was operated under conditions mimicking the typical detectors' experimental usage scenario, that is at a pressure of 1×10^{-5} mbar, cooled to −9 ° C and biased with a voltage of 200 V. After the 2 days long irradiation experiment the detector was stored at room temperature under ambient atmospheric conditions, and only powered and cooled again to the same conditions during post-irradiation follow-up performance measurements.

4.1 Detector performance characterization

We characterized the offset (mean dark signal), the root mean square (RMS) noise, the pixel-to-pixel variation of the signal amplification, the pixel averaged energy resolution and the absolute gain, i.e. the Analog Digital Unit (ADU) to energy conversion before and after irradiation. Particular attention was paid to be able to detect offset and noise changes with a sensitivity of 2%.

The detector offset is commonly defined as the average value of the dark signal of the detector. The detector noise, quantifying the variations of the dark signal relative to its mean, is calculated
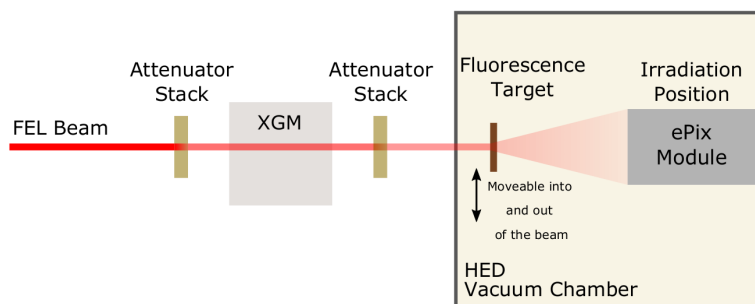
Figure 3. Experimental setup used to irradiate and calibrate the ePix100a detector module at the HED instrument (not to scale). The image shows the setup used for flat-field performance and calibration measurements (flat-field configuration). The attenuated beam is directed onto a copper target and the ePix100a module is shifted off the beam axis. The resulting fluorescence radiation illuminates the ePix100a module homogeneously. Since we used the copper target in a transmission geometry, the attenuated direct FEL beam is visible on the detector in addition to the copper fluorescence's photons (see figure 4). During irradiation measurements the ePix100a is facing the beam and the fluorescent target is moved out of the field of view of the ePix100a module (irradiation configuration). In both configurations the primary beam intensity is attenuated by two absorbing and configurable stacks located before and after the XGM.
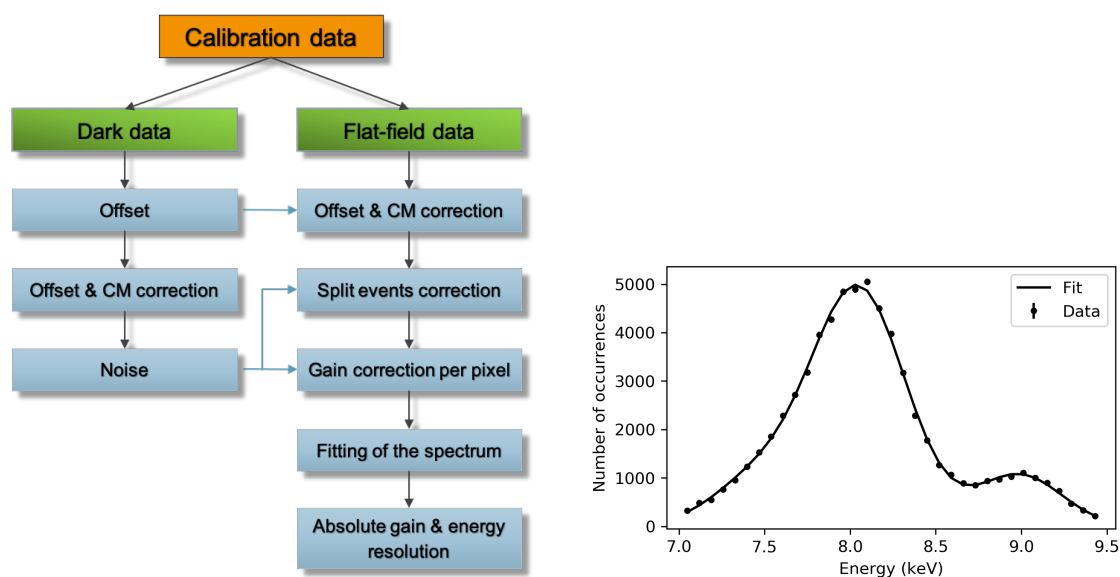

Figure 4. Left: flowchart illustrating the data correction steps applied to the dark and flat-field data and their sequence. Results derived from the analysis of the dark data are used as input for processing the flat-field data as illustrated by blue lines. Right: energy spectrum derived from flat-field data, showing the Cu-K$_\alpha$ fluorescence line blend at 8.041 keV, a line originating in photons of the FEL beam with an energy of 9 keV and a fit of three Gaussian peaks to the spectral data.

as the standard deviation of the measured dark signal. Variations in the voltage supplying the readout electronics can cause additional offset variations affecting groups of channels with a similar amplitude, this effect is known as common mode. For a detailed description of the nature of the components contributing to the dark signal and detector noise, we refer the reader to e.g. Knoll [32] and Lutz [33].

Flat-field data resulted from homogeneous irradiation of the ePix100a sensor area with copper fluorescence photons with an energy of $E_{K\alpha_1} = 8047.78\,\text{eV}$ and $E_{K\alpha_2} = 8027.83\,\text{eV}$, originating from a copper target installed in the FEL beam (see figure 3). Since the two Cu-K_{α_1} and Cu-K_{α_2} fluorescent lines cannot be resolved with the ePix100a detector, we observed instead a blend of lines with a yield weighted average energy of 8041.13 eV, to which we refer to as Cu-K_α lines in the remainder of this paper.

The procedure used for dark and flat-field data processing is outlined in figure 4. As the first step the per pixel offset $O_{x,y}$ is calculated as a mean signal for each pixel individually using 2000 images of the dark data. With an ASIC-, column- and row-wise common mode (CM) correction we removed signal baseline variations apparent in the dark data before calculating the RMS noise for each pixel. The common mode value is evaluated from the sorted vector S_i as

$$\bar{m}_k = \begin{cases} S_{(N-1)/2} & \text{for an odd number of pixels } N \\ \frac{1}{2}(S_{N/2} + S_{N/2+1}) & \text{for an even number of pixels } N, \end{cases} \tag{4.1}$$

where S_i is the signal measured in the pixel with the number i after offset subtraction, belonging to a specific ASIC area, one line or to one column numbered with k. This common mode value is subsequently subtracted from the signal of the pixels belonging to the area the common mode value was calculated from. Finally the RMS noise results from

$$\sigma_{x,y} = \sqrt{\frac{1}{N} \sum_{n=0}^{N-1} (c_{x,y,n} - \bar{c}_{x,y})^2}, \tag{4.2}$$

where $c_{x,y,n}$ is the offset and common mode subtracted dark signal measured in the pixels with column and line coordinates x and y of the image numbered n. The per-pixel average of the dark signal corrected for offset and common mode is denoted with $\bar{c}_{x,y}$. After applying the offset and a common mode correction to the flat-field data, we classified clustered signals of discrete photon events by the number of adjacent pixels where the charge is detected (split event/charge sharing correction, see [34, 35] for a more detailed description of the algorithm). To achieve the best possible energy resolution for subsequent spectral analysis, clusters of events with a pixel event multiplicity larger than one were rejected. A per-pixel gain correction removes small pixel-to-pixel variation of the characteristics of the pre-amplifiers implemented in each pixel. The data used for calculating the energy spectrum shown in figure 4 was treated in this way.

Fitting a model consisting of three Gaussian lines (two lines for modelling the two line peaks and one for the low energy shoulder of the Cu-K_α line peak) to the spectrum derived from the data of the ROI before irradiation yields the ADU to energy conversion factor (absolute gain) $g = (70.2 \pm 0.5)\,\text{eV/ADU}$ and an energy resolution of $(641 \pm 45)\,\text{eV}$ full width half maximum (FWHM). The spatial distribution of the noise and offset is consistent with a uniform distribution across the pixels inside the ROI, with a mean offset and RMS noise of 1756 ADU and 139 eV, the latter value corresponds to an equivalent noise charge (ENC) of $38\,\text{e}^-$.

4.2 Dose calibration

As described in section 4, we monitored the photon flux throughout our irradiation experiment with the XGM with an estimated uncertainty of 7 %. However, the XGM does not provide spatial information, i.e the intensity distribution of the beam profile with a position resolution equivalent or better than the spatial resolution of the ePix100a sensor. Instead, we determined the beam profile from direct beam measurements acquired at low X-ray intensities with the ePix100a. These measurements provided spatially resolved information about the beam shape and the position of the beam within the ROI.

Irradiating the detector with high intensity caused the directly irradiated pixel area to become unresponsive for the duration of the irradiation. The affected pixels provided a signal even significantly below the detected dark signal. The average value of the signal provided was 130 ADU. This effect is discussed in more detail in section 5. The position of the affected area on the sensor relative to the centre of the beam does not change over time. The importance of this effect lies in the possibility to track the position of the beam on the ePix100a sensor, enabling a calculation of the per-pixel dose in the presence of beam position jitter. By using the Canny edge detection algorithm [36] we determined the borders of the area with unresponsive pixels and assigned a circle to it. The centre of this circle provides the pixel coordinates of the beam core for each image frame individually. This procedure allows us to align the area with unresponsive pixels to the spatial beam distribution measured prior to the irradiation experiment and finally to reconstruct the number of photons delivered to individual ePix100a pixels with each pulse train as measured by the XGM. The per-pixel photon counts reconstructed for every ePix100a image frame and integrated over the duration of the irradiation results in the top left plot of figure 5.

Finally, we used the GEANT4 [37] based Monte Carlo simulation tool MULASSIS [38], originally developed for dose and particle fluence analysis of shielding materials, to estimate the absorbed dose in different depths of the ePix100a sensor, taking photoelectric absorption in the different sensor materials into account. These are specifically the aluminum entrance window, the silicon bulk and the SiO_2 layers in the pixel structure as outlined in figure 2. The output of the simulation is normalized to the dose deposited per primary photon and unit area cm^2, such that multiplying it with the measured per-pixel integrated photon number results in the total per-pixel dose. The resulting spatial distribution of the dose deposited in the sensor at the depth of the SiO_2 structures and integrated over the time of all irradiation cycles is shown in the top right image of figure 5. The horizontal asymmetry of the distribution has its origin in the horizontal motion of the beam spot during the course of the irradiation. The vertical cuts through the sensor shown in figure 5 illustrate the depth profile of the dose along the central column (bottom left image of figure 5) and row (bottom left image of figure 5).

While the region closest to the surface at the entrance window has received a maximum dose of (1.3±0.2) MGy at column number 10 and row number 9, the dose deposited at the depth of the SiO_2 structures is reduced by a factor of 240 to (5.4±0.7) kGy due to absorption by the sensor material above. This corresponds to a total dose of (180±13) MGy delivered to the surface of the sensor when neglecting absorption in the sensor material and integrating the dose over the spot profile. The dose received by the ASIC is further reduced by the shielding effect caused by the bump bonds. It can be estimated to < 24 kGy for the ASIC areas located below the bump bonds
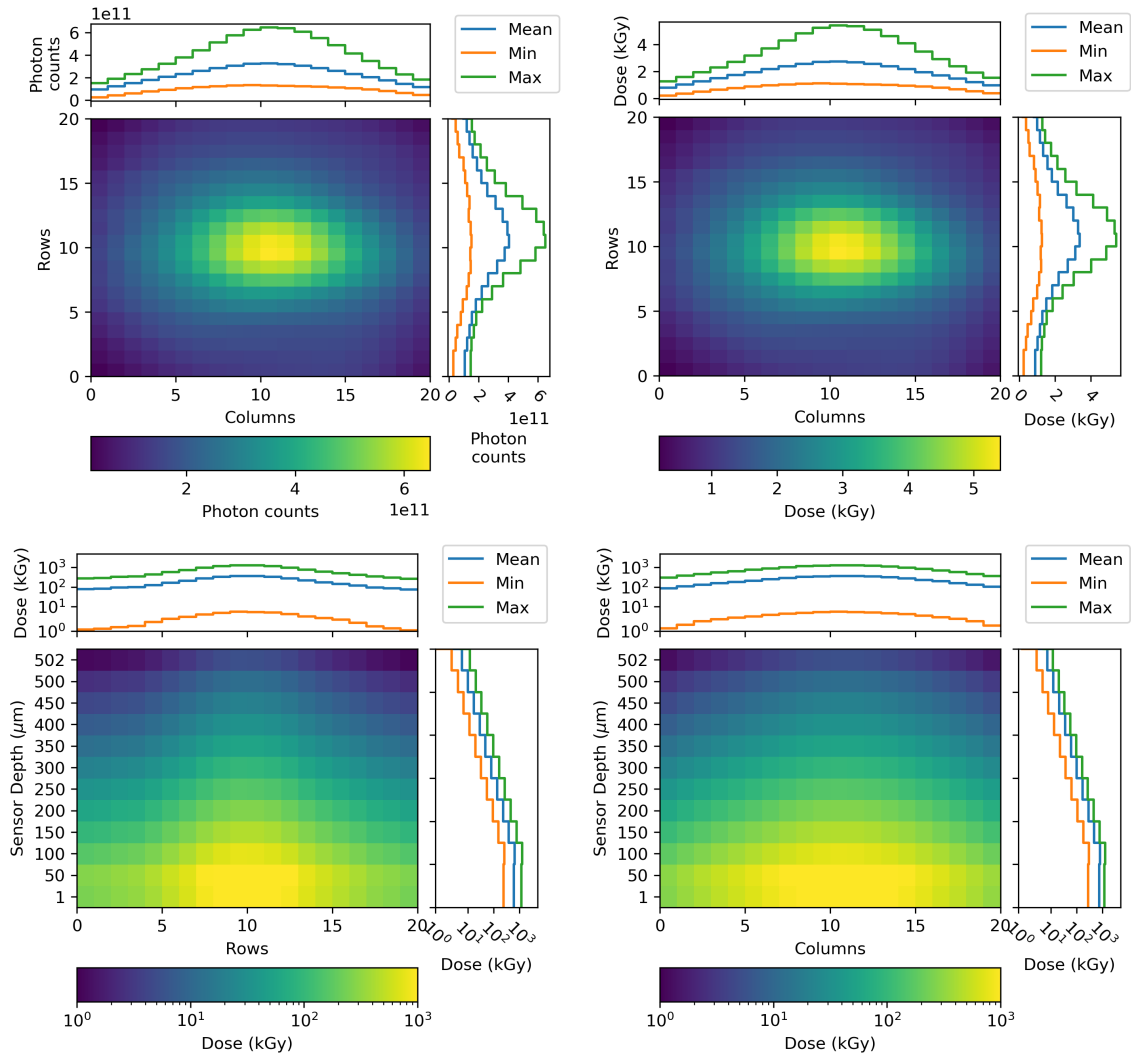
Figure 5. The top left plot shows the spatial distribution of the total number of photons in the region of interest integrated over the time of irradiation with the beam. The spatial distribution of the dose deposited at the depth of the SiO$_2$ layers is shown in the top right plot for the same region. The dose was simulated using the Monte Carlo simulation tool MULASSIS. The data shown on the top left side of this figure was used as input for the simulation. The bottom left corner of this picture corresponds to the bottom left corner of the region of interest marked as blue rectangle and being labelled "Irradiated Area" in figure 1. Bottom: depth profiles of the dose along column 10 (left) and row 9 (right) of the irradiated area. The orientation of the image is the same as the schematic view of the sensor shown in figure 2, i.e. the 1µm thick Aluminum entrance window is located at the bottom and the pixel structure on the top of the images. Please note that the dose values are shown on a linear scale in the top image and on a logarithmic scale in the bottom images. The panels on top and bottom of all images show minimum (orange), mean (blue) and maximum (green) values calculated along rows, columns or the sensor depth, respectively.

and to $(670 \pm 140)\,$kGy for the not shielded areas between the bump bonds. These numbers are translated to the surface of the ASIC, neglecting further structural details of the ASIC chip and absorption therein.

5 Experiment results

We characterized the pre- and post-irradiation performance of the ePix100a following the methodology as described in section 4. The observed offset, noise and gain changes can be categorized into immediate and post-irradiation effects. We observed immediate effects during irradiation on time scales shorter than seconds or minutes. With post-irradiation effects, we refer to changes of the detector performance on timescales of hours and days after the last irradiation cycle was completed. In the following sections, we describe both effect categories in detail.

5.1 Immediate effects

During irradiation with the high intensity FEL beam at an energy of $E_{\text{Beam}} = 1\,\mu$J, the pixels in the $20\,\text{pixels} \times 20\,\text{pixels}$ large ROI were unresponsive. We assume that this effect originates in the ASIC [23, 29]. There is no obvious mechanism at the silicon sensor that we are aware of, which could cause the signal of individual pixels to drop to such low values as 130 ADU on average. The mechanism by which this occurs has to be further investigated.

We would like to emphasise that the observed effect is of short duration and only present during irradiation. It does not lead to permanent damage: after irradiation, these pixels exhibit a dark signal saturating the detector's dynamic range, but their signal recovers to an offset level comparable to the surrounding pixels within the following 48 hours. Furthermore, these pixels are fully functional during dark signal measurements, as will be shown in the following.

With an increasing number of irradiation cycles, the number of pixels with an offset surpassing the upper end of the dynamic range of the ADC increased. The left part of figure 6 shows the situation shortly after the last irradiation cycle was completed. The pixels shown in yellow were completely saturated.

5.2 Post-irradiation and long term effects

5.2.1 Offset and noise

During the first three hours following the last irradiation cycle, the offset of individual pixels decreased exponentially with time with a decay coefficient of $-0.413\,\text{h}^{-1}$ as shown in the right part of figure 6 for $t_{\text{Int}} = 800\,\mu$s. The offset stabilized three days after irradiation at a higher level of 1832 ADU in comparison to the pre-irradiation level of 1762 ADU (see figure 7). As is evident from figure 7, the scale of this effect measured 3 days after irradiation remains the same also for the following measurements. In general, we observe a larger offset and corresponding ENC for $t_{\text{Int}} = 800\,\mu$s, when comparing pre- and post-irradiation conditions. Evaluating the offset change 46 days after irradiation, yielded an offset increase of approximately 15% for $t_{\text{Int}} = 800\,\mu$s and by 1% for $t_{\text{Int}} = 50\,\mu$s. The measured increase in offset scales linearly with the integration time, i.e. with a factor of $800\,\mu\text{s}/50\,\mu\text{s} = 16$, which is expected if the effect is predominantly due to an increase in dark current. As shown in figure 8 the ratio of offset change for two integration times

approaches the expected factor of 16 when the leakage current increases, which happens for doses above $\approx 4000\,$Gy. The figure can be divided into three regions, as illustrated by the dotted, solid and dashed lines. In the first region (dashed line) the contribution of the leakage current is negligible at $0\,$Gy, hence no difference in the offset between shorter and longer integration time exists and the observed ratio is 1. As the dose increases, the leakage current and in turn the ratio increases (second region, solid line). Finally, in the third region, the ratio approaches the ratio between the two integration times of 16 (dashed line), which is expected when the leakage current dominates.

As shown in the right part of figure 7, the RMS noise observed in these pixels follows the same behaviour. While the noise at $t_{\mathrm{Int}} = 800\,\mu$s has increased by 85%, for $t_{\mathrm{Int}} = 50\,\mu$s the increase is at the level of 30%. The maximal increase of the offset and noise 46 days after irradiation is measured for the average dose of $(4683 \pm 659)\,$Gy. The spatial distribution of the induced offset (left) and noise (right) changes is shown in figure 9 for $t_{\mathrm{Int}} = 800\,\mu$s.

Since different pixels within the ROI have received a different dose, we can evaluate the change of the offset and RMS noise between pre- and post-irradiation conditions depending on the dose, when assuming that the pixels inside the ROI react similarly to radiation-induced damage. Since the design of the pixels is the same and the observed pixel-to-pixel variations of the dark current, noise and amplification are $\approx 3\,\%$, we consider this assumption to be justified.

Figure 10 shows the offset (left) and noise (right) changes depending on the absorbed dose measured at the depth of the SiO_2 interface 46 days post-irradiation. Here again, the influence of the longer integration time is clearly visible. The slope derived from fitting a linear function to the data yields an offset and ENC change rate of $(56.0 \pm 0.6)\,$ADU/kGy and $(8.7 \pm 0.1)\,$e$^-$/kGy for $t_{\mathrm{Int}} = 800\,\mu$s and $(1.0 \pm 0.2)\,$ADU/kGy and $(2.0 \pm 0.1)\,$e$^-$/kGy for $t_{\mathrm{Int}} = 50\,\mu$s, respectively.
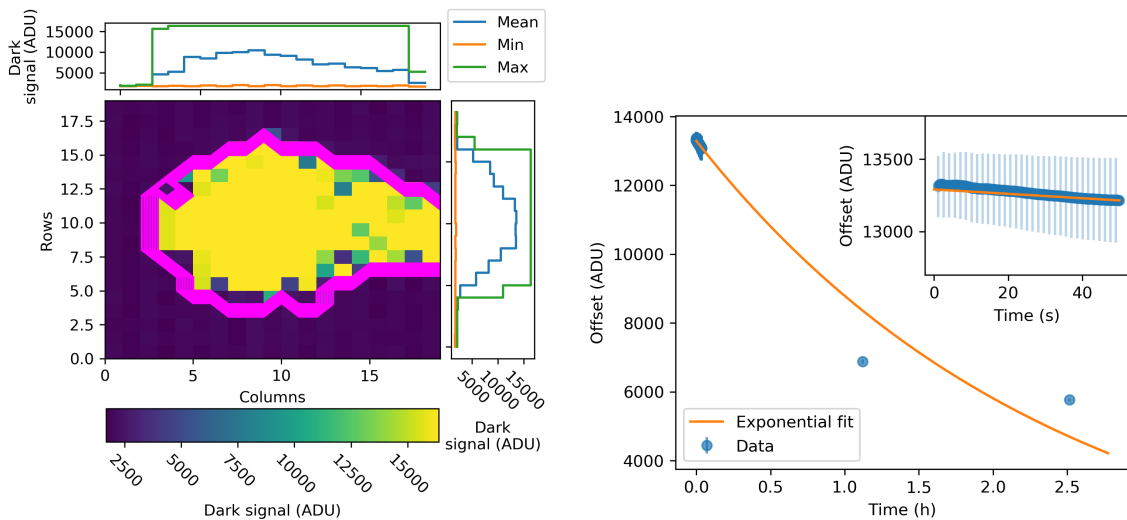

Figure 6. Left: image of the per pixel offset as observed in the ROI right after completion of the last irradiation cycle and after recovery from saturation. Pixels delivering an offset signal close or beyond the saturation threshold of the ADC have signal values > 15500 ADU (yellow color). Right: the evolution of the offset of those pixels located inside the magenta area in the figure on the left is shown. The evolution of the offset was monitored during two and a half hours after completion of the last irradiation cycle.
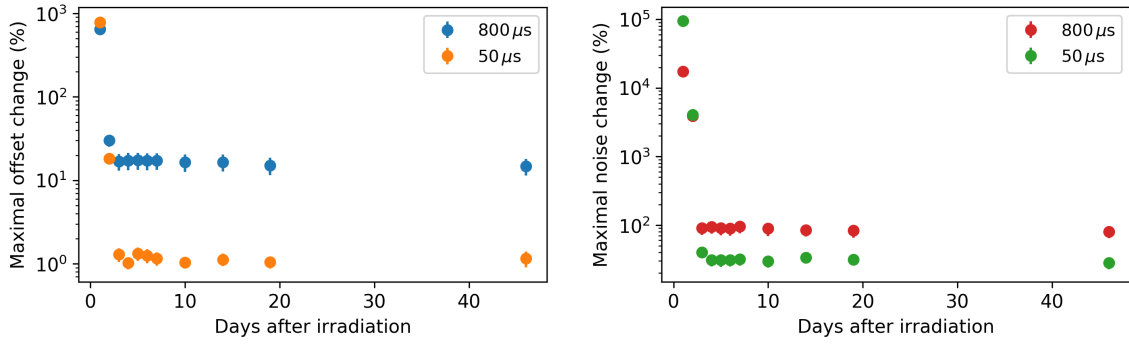
Figure 7. Left: evolution of the offset as observed in the pixel showing the highest relative offset increase for the two integration time settings, i.e. $t_{\text{Int}} = 50\,\mu\text{s}$ and $t_{\text{Int}} = 800\,\mu\text{s}$. The exponential decrease of the offset observed during the first day is followed by a stabilized state at higher offset values in comparison to the pre-irradiation level. Right: relative change of the noise as observed during the days following the last irradiation cycle. The temporal behaviour of the noise mirrors the temporal evolution of the offset. The average dose observed in the pixels showing the highest increase was $(4319 \pm 772)\,\text{Gy}$. The detector was kept at a temperature of $20\,°\text{C}$ between the individual measurements.
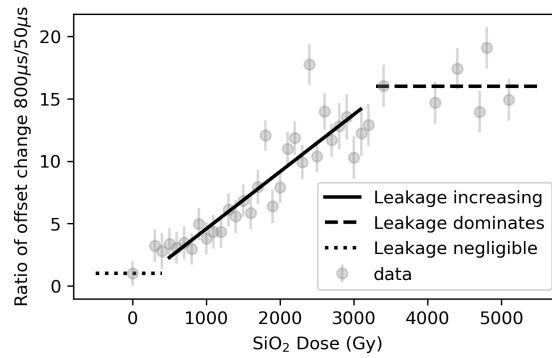

Figure 8. Ratio of the offset change measured at $800\,\mu\text{s}$ and $50\,\mu\text{s}$ (grey dots). The black dashed line shows the scaling factor of 16 expected from the ratio of the integration times when the leakage current dominates. If the leakage current is negligible the ratio equals 1 (dotted line.) The solid black line visualizes the region where the leakage current increases with the increasing dose.

If absorption of the radiation in silicon is neglected when calculating the dose, the offset and ENC change rate yields $(235.9 \pm 2.6)\,\text{ADU/MGy}$ and $(37.4 \pm 0.6)\,\text{e}^-/\text{MGy}$ for $t_{\text{Int}} = 800\,\mu\text{s}$ and $(4.2 \pm 0.6)\,\text{ADU/MGy}$ and $(8.3 \pm 0.4)\,\text{e}^-/\text{MGy}$ for $t_{\text{Int}} = 50\,\mu\text{s}$. The maximum observed increase of the offset reduces the available dynamic range of the detector by approximately 2% for $t_{\text{Int}} = 800\,\mu\text{s}$ and $\approx 0.1\%$ for $t_{\text{Int}} = 50\,\mu\text{s}$.

5.2.2 Gain and energy resolution

We took post-irradiation copper fluorescence flat-field data approximately one and a half hours after completion of the last irradiation cycle. At that time most of the pixels in the central part of the region of interest were still in saturation, thus not capable of detecting charge created by a photon interaction. Later, calibration measurements (with the detector in stabilized post-irradiation state)
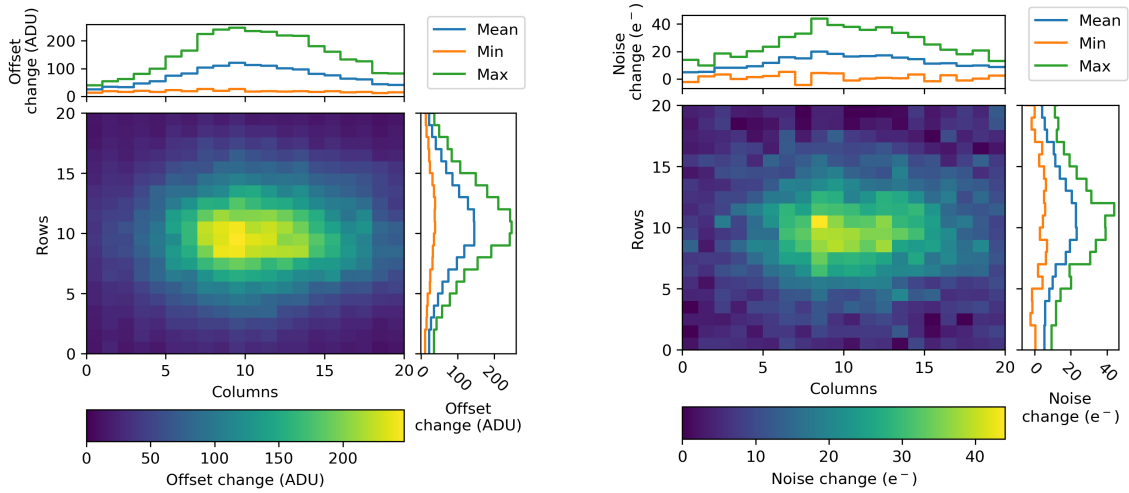
Figure 9. Radiation-induced changes of the offset (left) and noise (right) for $t_{Int} = 800\,\mu s$ evaluated 46 days after irradiation.
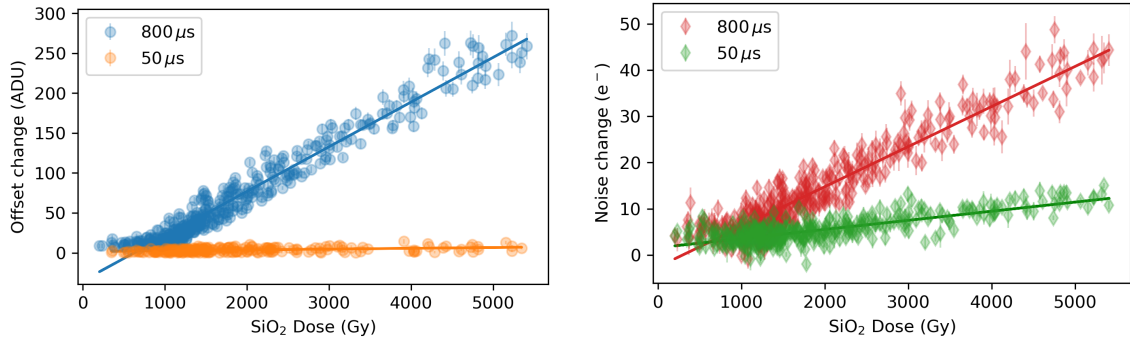

Figure 10. Left: the change of the offset observed in different pixels of the ROI 46 days after irradiation when comparing pre- and post-irradiation conditions depending on the accumulated dose at the depth of SiO_2 layers is shown for $t_{Int} = 50\,\mu s$ and $t_{Int} = 800\,\mu s$. Right: dependency of the ENC observed in different pixels of the ROI on the accumulated dose in units of electrons for the same integration time setting.

were not possible due to time-constrained access to the instrument. In order to characterise the gain and energy resolution, we, therefore, used pixels located in the periphery of the saturated area to compare the pre- and post-irradiation performance.

The left part of figure 11 shows a comparison of the measured spectrum of the Cu-K$_\alpha$ lines and the 9 keV line resulting from the photon beam before (black) and after irradiation (red) calculated from the peripheral pixels in the region of interest. The FWHM of the lines is larger after irradiation and the lines have a more pronounced low energy tail.

Figure 11 on the right shows the dependency of the peaks' FWHM on the dose accumulated by each individual pixel. We find an increase of the FWHM of 100 eV per 866 Gy. Following the relation of the intrinsic resolution limit of a semiconductor detector $\Delta E \propto \sqrt{FWE}$, with the Fano factor $F = 0.120$, the photon energy E and the energy required to create an electron-hole pair $W = 3.66\,eV$ [39, 40], we would expect the behaviour indicated by yellow squares (labeled

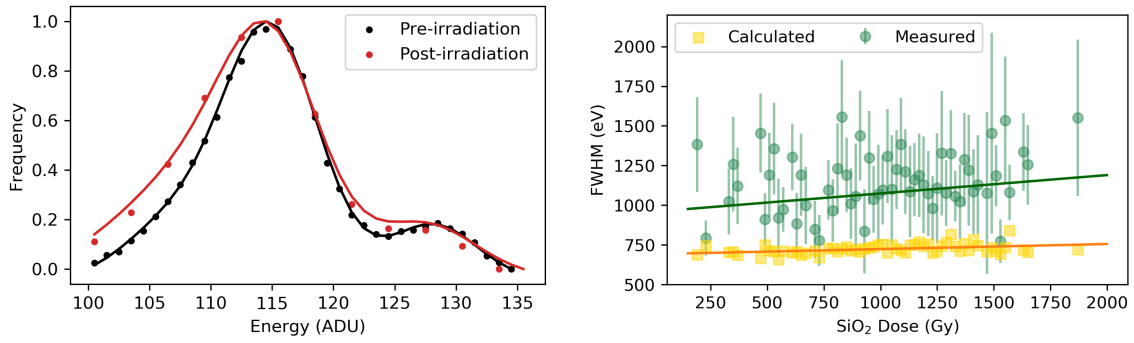**Figure 11**. Left: the spectral distribution of the Cu-K$_\alpha$ photons and 9 keV photon peak as detected by pixels in the periphery of the region of interest before irradiation (black) and after irradiation (red). Right: relation of the Cu-K$_\alpha$ line peak width (assessed as FWHM) to the dose absorbed in the SiO$_2$ layer. Values extracted from measurement are marked with green dots, while the yellow squares shows the expected FWHM calculated from the noise in pixels.

as "Calculated"). The increase of the FWHM values follows the same slope (within the estimated errors) as the calculated intrinsic resolution values. The intercept values of the linear models are separated by 184 eV (best case scenario including 1 σ uncertainties), which is approximately consistent with the increased mean noise value measured in the peripheral pixels of the region of interest after irradiation. These results suggest, that the observed broadening of the Cu-K$_\alpha$ line is driven by the radiation-induced noise increase. It is to note that in order to convert ADU values to eV/e$^-$ units a pre-irradiation absolute gain value of $g = (70.2 \pm 0.5)$ eV/ADU was used.

Before irradiation, we find (114.75 ± 0.07) ADU for the position of the Cu-K$_\alpha$ line blend. Figure 12 shows the position of the Cu-K$_\alpha$ line extracted from single pixel spectra of irradiated pixels in dependence of the absorbed dose. Applying a linear model to the data yields a slope which is consistent with 0, indicating no change of the Cu-K$_\alpha$ line position with dose. The Cu-K$_\alpha$ line after irradiation is located at (113.62 ± 0.37) ADU as we determined from the linear model.
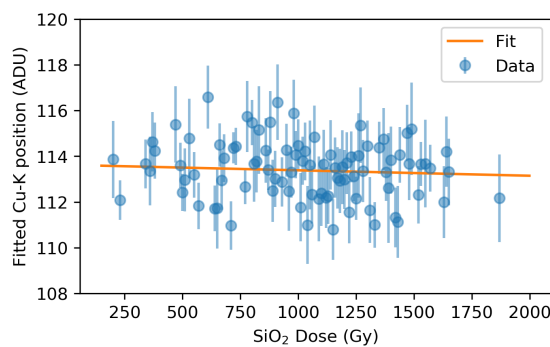

Figure 12. Position of the Cu-K$_\alpha$ line in dependency of an accumulated dose in different pixels. The line position was determined by fitting our Gaussian model to the spectra.

Since the flat-field calibration measurement contained only pixels with an absorbed dose up to a maximum of 2 kGy, the gain behaviour for the most irradiated pixels could not be studied. In

order to study the gain behaviour of these pixels, we performed a charge injection scan with the current sources implemented in each pixel 240 days after irradiation. During the linearity scan, an increasing signal is injected into a preamplifier with an internal 10-bit pulser, thus simulating a charge created by photon interactions in the sensor material. For our measurement, 1024 steps of the pulser were used to scan the full dynamic range of the detector.

The observed gain values derived from Cu-K$_\alpha$ fluorescence data are shown in dependency of the absorbed dose in the left part of figure 13. The x-axis range is limited to dose values below 2 kGy, as the pixels which have seen a higher dose were still saturated at the time the flat-field data was taken (see section 5.1). The slope $(-2 \pm 9) \times 10^{-5}$ ADU keV^{-1}Gy^{-1} derived from a linear model fitted to the data is consistent with zero, indicating that the gain is not changing significantly up to a dose of ≈ 2 kGy. This behavior changes as soon as higher dose levels are reached. If we take the charge injection data covering the range between 2750 Gy and 5500 Gy into consideration (right part of figure 13), we find the gain decreasing with the rate of $(-6 \pm 3) \times 10^{-5}$ ADU keV^{-1}Gy^{-1} as indicated by the black solid line in the right panel of figure 13. Gain values for lower deposited dose, i.e. deposited dose ≤ 2600 ADU do not show a decrease as shown by the dashed red line. The significance of the gain decrease with higher doses is visualised by residuals of a constant function fitted to charge injection data up to a dose of 2600 Gy and extended to the full range of deposited doses. As shown by the red dots in the residuals plot in figure 13, the gain values for doses above 4 kGy deviate up to -3σ, thus indicating a weak gain decrease. On the other hand, the residuals visualized by black dots corresponding to the linear fit to gain values for doses above 2750 Gy show a very good agreement between the measured values and the fitted function.
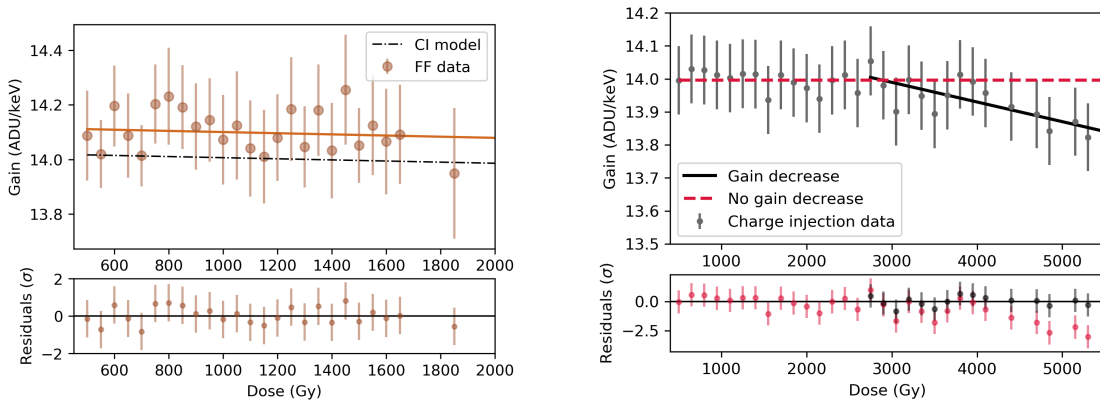

Figure 13. Left: gain estimated from the Cu-K$_\alpha$ fluorescence data depending on dose. The black line shows a model derived from charge injection data (marked as "CI model") estimated for the absorbed dose in the range of 500 Gy and 2600 Gy. Right: gain calculated from the internal charge injection data in relation to the absorbed dose. Two regions were fitted separately, lower dose region (≤ 2600 Gy) where no gain decrease is observed and higher dose region (> 2600 Gy) showing a weak gain decrease. Residuals (red dots) of the constant function extended to the whole deposited dose range show a systematic deviation from the charge injection data of up to -3σ for gain values above ≈ 4 kGy. Hence, demonstrating a weak gain decrease.

6   Interpretation

We attribute the measured increase of the leakage current and consequently higher offset after irradiation to radiation-induced damage in the sensor by a mechanism discussed by Schwandt et al. [10]. The generation of $e^- - h$ pairs close to the Si-SiO$_2$ interface and build up of positive charge lead to high electric fields near the interface causing changes to the depletion boundary. Coulomb repulsion happening between positively doped boron implantation and positive charges accumulating near the oxide layer might result in a shrinking of the boron implanted region on its edges, thus exposing the metal contact and allowing the depleted area to extend to the region close to the metal contact. Potentially, the bending of the depletion boundary can reach the edges of the metal contact and thus increase the electron leakage current. When the generation of new charge carriers is interrupted, the recombination process dominates and the leakage current will decrease exponentially as observed and shown in the right part of figure 6.

The effects on the gain were found to be pronounced at higher doses and are visible in the charge injection scan data. This indicates a radiation effect on the readout electronics in the ASIC, as the sensor-induced signal does not significantly contribute to those measurements. We see different mechanisms which could lead to such an observed gain decrease. However, presently, it is not fully understood which of these mechanisms contribute to the gain change observed in the ASIC.

To explain the gain changes and pixel saturation, both of which occur on an ASIC-level in more detail, a device simulation based on the specific design of the ePix100a sensor would be required, which is beyond the scope of this work.

7   Detector lifetime estimate

The radiation-induced damage presented in the previous section can be used to estimate the lifetime of the detector depending on the beam energy used during experiments and limits for the measurement time beyond which the performance of the detector will significantly degrade. The estimates presented here are based on the extrapolation of the measured relationship of the induced damage and dose absorbed in the SiO$_2$ layer.

Figure 14 illustrates the time needed for a specific dynamic range reduction depending on the beam energy. A reduction of the dynamic range by 50% can be expected at a dose of ca. (131±18) kGy for $t_{\text{Int}} = 800\,\mu s$ and at ca. (7.4±1.0) MGy for $t_{\text{Int}} = 50\,\mu s$ absorbed in a maximally irradiated pixel. Assuming a beam spatial distribution similar to the one used during this radiation damage experiment, i.e. the most irradiated pixel receiving 1% of the total beam energy, the dose per 20 pixels × 20 pixels area amounts to ca. (13±1) MGy for $t_{\text{Int}} = 800\,\mu s$ and (740±64) MGy for $t_{\text{Int}} = 50\,\mu s$. Saturation of the ADC dynamic range will occur at (262±36) kGy ($t_{\text{Int}} = 800\,\mu s$), respectively at (14.8±2.0) MGy ($t_{\text{Int}} = 50\,\mu s$), i.e. at (26±2) MGy ($t_{\text{Int}} = 800\,\mu s$) and at (1.48±0.13) GGy ($t_{\text{Int}} = 50\,\mu s$) of the total absorbed dose in ROI. The left panel of figure 14 shows three exemplary cases for the expected dynamic range behaviour; dynamic range reduction as observed in this radiation hardness study (blue dots), extrapolated loss of 50% of the ADC range (orange dots) and saturation of the ADC dynamic range due to the leakage current (green dots) for 800 μs integration time. The same cases are plotted for $t_{\text{Int}} = 50\,\mu s$ on the right. The lowest beam energy shown in both graphs corresponds to an energy deposited to the detector which is equivalent
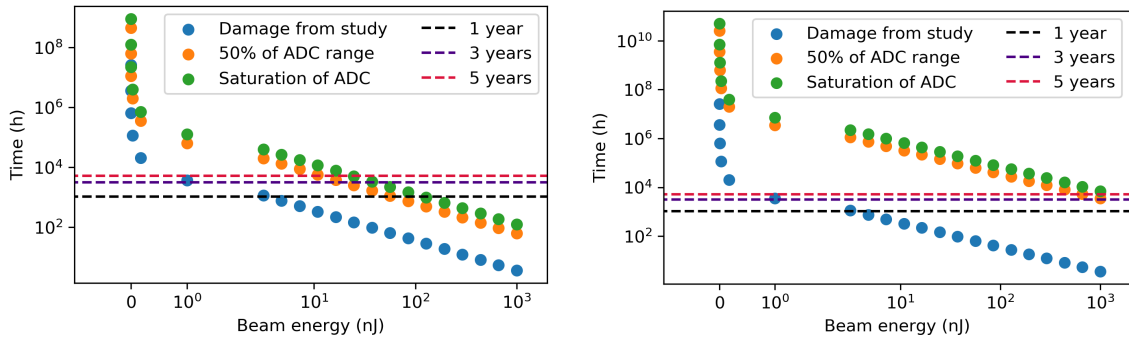
Figure 14. Estimate of time needed to reach specific level of the dynamic range reduction at a certain beam energy. Three scenarios are shown; the reduction level observed during this radiation hardness study (blue dots), reduction to 50 % of the initial dynamic range (orange dots) and complete saturation of the ADC by the leakage current (green dots). The left plot shows the estimate for $t_{Int} = 800\,\mu s$ and the right plot is for $t_{Int} = 50\,\mu s$.

to the upper limit of the ePix100a dynamic range within one integration cycle, i.e. 100 photons at 8 keV. For estimate, we assumed that photons are impinging mostly the same region of the detector during scientific experiments. This assumption is reasonable for small angle scattering experiments. As an example, the horizontal lines in both plots visualize the number of hours the detector can be exposed to the beam during one, three and five years of operation at the European XFEL to reach the corresponding dynamic range reduction. For our estimate, we assumed 4216 hours of beam time operation per calendar year at the European XFEL. This value corresponds to the planned X-ray delivery time for the year 2021. As one beamline serves two scientific instruments, the allocated time is assumed to be shared equally between the two. Moreover, we estimate the detector to be exposed to X-rays only 50% of the available time, i.e. the detector will be exposed to radiation for 4216 h/year×0.5×0.5 = 1054 h/year. Hence the black line visualizing the dynamic range reduction during one year of operation corresponds to 1054 hours of a beam on the detector. The numbers presented in figure 14 are of general nature and can be transferred to any other usage scenario, e.g. at other X-ray facilities. Significant reduction of the dynamic range is not expected, if the detector is illuminated with a beam energy below the dynamic range of the ADC, i.e. $\leq 100{\times}8$ keV photons.

The ePix100a detector was designed for low noise spectroscopy applications, hence requiring single photon sensitivity, i.e. good photon-to-noise discrimination down to the lowest photon energies. In this context, the detector's noise is an important performance parameter. A common requirement for imaging detectors used at FEL facilities is a false hit detection probability per megapixel area, i.e. $P(0|1) < 10^{-6}$, which corresponds to a photon peak-to-noise separation of approximately $5\,\sigma$ at a given energy. The lowest acceptable signal-to-noise value is usually considered to be $3\,\sigma$. Figure 15 shows the evolution of the signal to noise ratio if the detector is exposed to a given beam energy for a specific amount of time. The $5\,\sigma$ (cyan) or $3\,\sigma$ (magenta) peak separation are indicated for a photon energy of 9 keV. The plot on the left shows the separation power reduction at 800 μs integration time and the right plot at the integration time of 50 μs. As in the previous figure, the horizontal lines mark the beam time hours at the European XFEL per calendar year. A critical noise increase, hence reduction in peak-to-noise separation is only expected at beam intensities above the detector's dynamic range. Irradiating the detector for 2 years with an
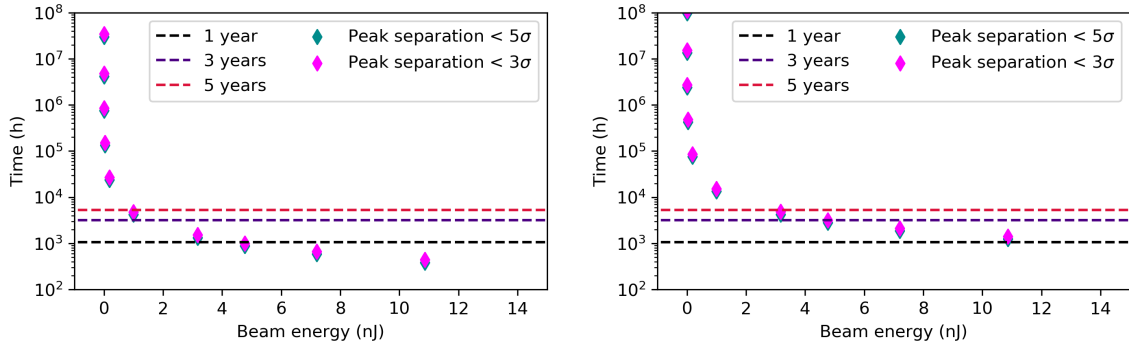
Figure 15. Estimate of time needed to reduce a peak-to-noise separation power below $5\,\sigma$ (green) and $3\,\sigma$ (pink) for $t_{Int} = 800\,\mu s$, shown on the left plot and for $t_{Int} = 50\,\mu s$, shown on the right in dependency of the used beam energy.

Table 2. Estimated dose thresholds above which a significant degradation of the detectors' performance will occur, i.e. a reduction of its dynamic range and peak separation power.

	Dose absorbed in SiO_2			
Integration time	ADC range reduction		Peak separation	
	50 %	100 %	$< 5\,\sigma$	$< 3\,\sigma$
50 μs	(7.4 ± 1.0) MGy	(14.8 ± 2) MGy	(28 ± 4) kGy	(32 ± 4) kGy
800 μs	(131 ± 18) kGy	(262 ± 36) kGy	(9 ± 1) kGy	(10 ± 1) kGy

energy of 2.5 nJ would cause a drop of the signal-to-noise ratio below $3\,\sigma$ at 800 μs integration time, while at 50 μs the same energy during 5 years would lead to a drop below $5\,\sigma$. The dose deposited to the SiO_2 layers delivered to the area of 20 pixels × 20 pixels resulting from the beam energy of 2.5 nJ corresponds to (1.1 ± 0.1) GGy. The same beam energy leads to a dose of (2.7 ± 0.2) GGy in 5 years. The beam energy needed to worsen the peak-to-noise separation below $5\,\sigma$ in 5 years of operation at 800 μs integration time is ≈ 0.4 nJ, which exceeds the dynamic range of the ePix100a by ≈ 3 orders of magnitude. Table 2 summarizes the dose thresholds deposited at the SiO_2 above which the detector's dynamic range and peak separation power will degrade.

8 Conclusions & outlook

We have performed a systematic study of the influence of radiation-induced damage on the performance of the ePix100a detector. We irradiated the ePix100a detector under controlled conditions with the direct and attenuated European XFEL beam with X-ray photons with an energy of 9 keV and a beam energy of 1 μJ. Pixels irradiated by this energy do not show a signal-dependent response upon irradiation but remain functional under normal operating conditions. Irradiating the detector beyond the beam energy of 1 μJ for longer time periods, e.g. > 5 min will cause failure of the irradiated pixels. Furthermore, we provide irradiation limits for typical usage scenarios at the European XFEL, which results in a certain damage level. Our results can be transferred to experimental conditions at other facilities and experiments.

The irradiated area of $1\,mm^2$ has received a dose of approximately $760\,kGy$ at the depth of Si/SiO_2 in the sensor, which corresponds to $180\,MGy$ delivered to the surface of the sensor. The dose-dependent increase of the offset and noise is mainly caused by an increase of the leakage current. The observed broadening of the $Cu\text{-}K_\alpha$ fluorescence line measured $90\,min$ post-irradiation is scaling with the increasing noise in the pixels and thus is caused by the radiation-induced leakage current. A change of the gain is not expected for a dose $< 4\,kGy$. Nevertheless, a charge injection scan showed a weak gain decrease for the most irradiated pixels and suggests a weak damage occurring at the pixel preamplifier. Single photon discrimination at a significance level of $> 5\,\sigma$ can be achieved with the ePix100a up to a dose of $9\,kGy$ at $t_{Int} = 800\,\mu s$ and up to $28\,kGy$ at $t_{Int} = 50\,\mu s$.

In the near future, we plan to investigate sensor annealing as a possibility to mitigate the radiation-induced performance changes to conclude the ePix100a radiation hardness study.

References

[1] W. Decking et al., *A MHz-repetition-rate hard X-ray free-electron laser driven by a superconducting linear accelerator*, *Nature Photon.* **14** (2020) 391.

[2] H. Graafsma, *Requirements for and development of* 2 *dimensional X-ray detectors for the European X-ray free electron laser in Hamburg*, 2009 *JINST* **4** P12011.

[3] M. Kuster et al., *Detectors and calibration concept for the European XFEL*, *Synchrotron Radiat. News* **27** (2014) 35.

[4] J. Zhang, E. Fretwurst, H. Graafsma, R. Klanner, I. Kopsalis and J. Schwandt, *Study of X-ray radiation damage in the AGIPD sensor for the European XFEL*, 2014 *JINST* **9** C05022 [arXiv:1312.3928].

[5] A. Koch et al., *Performance of an LPD prototype detector at MHz frame rates under synchrotron and FEL radiation*, 2013 *JINST* **8** C11001 [arXiv:1311.1688].

[6] J.H. Jungmann-Smith et al., *Radiation hardness assessment of the charge-integrating hybrid pixel detector JUNGFRAU* 1.0 *for photon science*, *Rev. Sci. Instrum.* **86** (2015) 123110.

[7] G. Blaj et al., *X-ray detectors at the linac coherent light source*, *J. Synchrotron Radiat.* **22** (2015) 577.

[8] J. Zhang et al., *Study of X-ray radiation damage in silicon sensors*, 2011 *JINST* **6** C11013 [arXiv:1111.1180].

[9] J. Zhang, E. Fretwurst, R. Klanner, I. Pintilie, J. Schwandt and M. Turcato, *Investigation of X-ray induced radiation damage at the Si-SiO₂ interface of silicon sensors for the European XFEL*, 2012 *JINST* **7** C12012 [arXiv:1210.0427].

[10] J. Schwandt, E. Fretwurst, R. Klanner, I. Pintilie and J. Zhang, *Optimization of the radiation hardness of silicon pixel sensors for high X-ray doses using TCAD simulations*, 2012 *JINST* **7** C01006 [arXiv:1111.4901].

[11] J. Schwandt, E. Fretwurst, R. Klanner, I. Kopsalis and J. Zhang, *Design and first tests of a radiation-hard pixel sensor for the European X-ray Free-Electron Laser*, *IEEE Trans. Nucl. Sci.* **61** (2014) 1894.

[12] R. Klanner et al., *Challenges for silicon pixel sensors at the European XFEL*, *Nucl. Instrum. Meth. A* **730** (2013) 2 [arXiv:1212.5045].

[13] A. Allahgholi et al., *The adaptive gain integrating pixel detector at the European XFEL*, *J. Synchrotron Radiat.* **26** (2019) 74.

[14] A. Affolder et al., *Silicon detectors for the sLHC*, *Nucl. Instrum. Meth. A* **658** (2011) 11.

[15] G. Lindström, *Radiation damage in silicon detectors*, *Nucl. Instrum. Meth. A* **512** (2003) 30.

[16] J. Bourgoin, P. Ludeau and B. Massarani, *Threshold energy determination in thick semiconductor samples*, *Rev. Phys. Appl.* **11** (1976) 279.

[17] E. Holmström, A. Kuronen and K. Nordlund, *Threshold defect production in silicon determined by density functional theory molecular dynamics simulations*, *Phys. Rev. B* **78** (2008) 045202.

[18] C. Gößling, C. Lichau, M. Peters, J. Wüstenfeld and R. Wunstorf, *Influence of surface damage on highly segmented silicon detectors*, *Nuovo Cim. A* **112** (1999) 1369.

[19] F.B. McLean and T.R. Oldham, *Basic mechanisms of radiation effects in electronic materials and devices, final report, September* 1986–*September* 1987, Tech. Rep. AD-A-186936/1/XAB, Harry Diamond Labs, Adelphi, MD, U.S.A. (1987).

[20] T. Ma and P.V. Dressendorfer, *Ionizing radiation effects in MOS devices and circuits*, John Wiley & Sons, New York, NY, U.S.A. (1989).

[21] T.R. Oldham, *Ionizing radiation effects in MOS oxides*, volume 3, World Scientific, Singapore (1999).

[22] G. Blaj et al., *X-ray imaging with ePix100a: a high-speed, high-resolution, low-noise camera*, *Proc. SPIE* **9968** (2016) 99680J.

[23] B. Markovic et al., *Design and characterization of the ePix100a: a low noise integrating pixel ASIC for LCLS detectors*, *IEEE Nucl. Sci. Symp. Med. Imag. Conf. Rec.* (2014) 1.

[24] K. Nishimura et al., *Design and performance of the ePix camera system*, *AIP Conf. Proc.* **1741** (2016) 040047.

[25] HED, *Scientific instrument HED. EuXFEL webpage*, https://www.xfel.eu/facility/instruments/hed/index_eng.html.

[26] MID, *Scientific instrument MID. EuXFEL webpage*, https://www.xfel.eu/facility/instruments/mid/index_eng.html.

[27] A. Madsen et al., *Materials Imaging and Dynamics (MID) instrument at the European X-ray Free-Electron Laser facility*, *J. Synchrotron Radiat.* **28** (2021) 637.

[28] T. Koyama et al., *Investigation of ablation thresholds of optical materials using* 1 µ*m-focusing beam at hard X-ray Free Electron Laser*, *Opt. Express* **21** (2013) 15382.

[29] G.A. Carini et al., *Characterization of the eLine ASICs in prototype detector systems for LCLS*, *IEEE Nucl. Sci. Symp. Med. Imag. Conf. Rec.* (2012) 515.

[30] T. Maltezopoulos et al., *Operation of X-ray gas monitors at the European XFEL*, *J. Synchrotron Radiat.* **26** (2019) 1045.

[31] A.A. Sorokin et al., *An X-ray gas monitor for free-electron lasers*, *J. Synchrotron Radiat.* **26** (2019) 1092.

[32] G.F. Knoll, *Radiation detection and measurement*, John Wiley & Sons, New York, NY, U.S.A. (2011).

[33] G. Lutz, *Semiconductor radiation detectors*, Springer, Berlin, Heidelberg, Germany (2007).

[34] M. Kuster et al., *The* 1*-megapixel pnCCD detector for the small quantum systems instrument at the European XFEL: system and operation aspects*, *J. Synchrotron Radiat.* **28** (2021) 576.

[35] EuXFEL, *XFEL detector tools' documentation*, European XFEL GmbH, (2020).

[36] J. Canny, *A computational approach to edge detection*, *IEEE Trans. Pattern Anal. Machine Intell.* **8** (1986) 679.

[37] M. Pia, *The GEANT*4 *toolkit: simulation capabilities and application results*, *Nucl. Phys. B Proc. Suppl.* **125** (2003) 60.

[38] F. Lei et al., *MULASSIS: a GEANT4-based multilayered shielding simulation tool*, *IEEE Trans. Nucl. Sci.* **49** (2002) 2788.

[39] B. Lowe and R. Sareen, *A measurement of the electron-hole pair creation energy and the Fano factor in silicon for* 5.9 *kev X-rays and their temperature dependence in the range* 80–270 *K*, *Nucl. Instrum. Meth. A* **576** (2007) 367.

[40] M. Mazziotta, *Electron-hole pair creation energy and Fano factor temperature dependence in silicon*, *Nucl. Instrum. Meth. A* **584** (2008) 436.